RSC Advances

PAPER

View Article Online
View Journal | View Issue

Cite this: *RSC Adv.*, 2020, **10**, 19192

Tuning nanocavities of Au@Cu_2O yolk–shell nanoparticles for highly selective electroreduction of CO_2 to ethanol at low potential†

Bin-Bin Zhang, Ya-Hui Wang, Shan-Min Xu, Kai Chen, Yu-Guo Yang* and Qing-Hua Kong *

Received 17th March 2020
Accepted 12th May 2020

DOI: 10.1039/d0ra02482a

rsc.li/rsc-advances

The electrosynthesis of high-value ethanol from carbon dioxide and carbon monoxide addresses the need for the large-scale storage of renewable electricity and reduction of carbon emissions. However, the electrosynthesis of ethanol by the CO_2 reduction reaction (CO_2RR) has suffered from low selectivity and energy efficiency. Here, we report a catalyst composed of Au nanoparticles in Cu_2O nanocavities (Au@Cu_2O) that is very active for CO_2 reduction to ethanol through the confinement of the CO intermediate. The architecture shows tandem catalysis mechanisms in which CO_2 reduction on Au yolks produces CO filling Cu nanocavities, where a sufficiently high CO concentration due to the confinement effect promotes ethanol formation and then results in an ethanol faradaic efficiency of 52.3% at −0.30 V *versus* the reversible hydrogen electrode (*vs.* RHE) *via* regulating the hollow size of the Cu_2O nanocavities. Such a strategy provides a new way of fabricating various tandem catalysts with high selectivity and efficiency for the CO_2RR.

Introduction

The electrocatalytic reduction of CO_2 to valuable carbon-based fuels and chemicals offers a route to reduce CO_2 emissions and facilitate the long-term storage of renewable electricity.[1–6] In particular, C_2 and C_{2+} products from the CO_2 reduction reaction (CO_2RR) have attracted considerable attention due to their relatively high energy density, added-value and widespread use as feedstocks in polymer synthesis, *etc.*[7–9] Excellent electrocatalysts have been developed to boost the activity and selectivity of the CO_2RR towards C_2 and C_{2+} productions.[10–14] Among currently available materials, Cu-based catalysts have been reported as the most promising electrodes for producing C_2 and C_{2+} compounds under aqueous conditions in CO_2RR, and have been extensively studied.[8,12,15–21] However, there still present some scientific challenges, such as poor selectivity, low faradaic efficiency and durability, which need to be managed primarily in further work.

To date, several avenues have been employed to improve the selectivity of Cu-based catalysts for CO_2RR to specific products, including altering size, structure, composition, surface state, and so on.[17–20] Hori *et al.* declared that the product selectivity of CO_2RR shifted greatly with the crystal orientation, where Cu(100) yielded mainly C_2H_4 and Cu(111) benefited CH_4 production.[22] Sargent's group constructed a core–shell vacancy engineering catalyst (Cu_2S–Cu–V) to steer products beyond alkenes and toward ethanol at certain potentials.[23] More recently, theoretical and experimental investigations demonstrate that the activity and selectivity for C_2 and C_{2+} of Cu-based catalysts can be greatly advanced by bimetallic strategy or constraining the local CO concentration at the catalyst–electrolyte interface.[24,25] Au/Cu bimetallic electrocatalyst was obtained with improved activity and selectivity for electrochemical transformation of CO_2 to alcohols over hydrocarbons at low overpotentials, and a tandem catalysis mechanism has been proposed where Au nanoparticles (Au NPs) reduce CO_2 to CO near the copper surface, driving a high CO coverage.[25] When supplied directly with CO instead of CO_2 as a feedstock, oxide-derived nanocrystalline copper electrodes produce ethanol with up to 30% faradaic efficiency at modest overpotentials under alkaline conditions.[26] In addition, the confinement effect is known to alter thermodynamic and transport properties of fluids.[27–30] Prior studies of porous catalysts exploited confinement effect to implement a selectivity shift by extending the retention of C_1 or C_2 species, and then boost C_2 or C_3 production,[16,24] which lack in-depth exploration. As such, developing a new strategy of combining bimetallic strategy and confinement effect is highly imperative for boosting the selectivity to ethanol in CO_2 electroreduction and its practical application.

Herein, we further apply the confinement effect with a bimetallic yolk–shell structure of Au nanoparticle in Cu_2O nanocavity (Au@Cu_2O), whereas Au shows high catalytic activity for converting CO_2 to CO at low potentials,[31,32] and Cu is able to

Department of Chemistry, School of Science, Beijing Jiaotong University, Beijing 100044, China. E-mail: ygyang@bjtu.edu.cn; qhkong@bjtu.edu.cn

† Electronic supplementary information (ESI) available. See DOI: 10.1039/d0ra02482a

catalyze the second step of the tandem reaction, the reduction of CO to C_2 products at low potentials.[33–35] The Au@Cu_2O catalyst has higher selectivity for ethanol compared with hydrocarbons at lower overpotentials. We propose that the selectivity shifting from C_1 to C_2 originates from a tandem catalysis mechanism, where Au NPs reduce CO_2 to CO in the Cu nanocavities, producing a high CO concentration, thus boosts the ethanol production due to the confinement of CO intermediate. Meanwhile, we adjust the CO concentration in the nanocavities by regulating the hollow size of the Cu_2O nanocavities, and then achieve an ethanol faradaic efficiency of 52.3% at −0.30 V *vs.* RHE.

Experimental

Chemicals

Hydrogen tetrachloroaurate(III) trihydrate ($HAuCl_4 \cdot 3H_2O$, 99.99%), citric acid, trisodium salt (98%), copper(II) nitrate trihydrate (99%), hydrazine hydrate (hydrazine, 64%), polyvinylpyrrolidone (PVP, average M.W 58000), 2-propanol (99.7+%), Nafion (5%). All chemicals were obtained directly without further purification.

Preparation of Au NPs

The Au NPs with a diameter of about 22 ± 2 nm were synthesized and used as the core materials for the Au@Cu_2O yolk–shell particle fabrication.[36,37] Au NPs were prepared by a standard citrate reduction procedure. Typically, 150 mL of 0.025 M $HAuCl_4$ solution was added into a three-necked round bottom flask and heated to boiling under continuously magnetic stir with condensing and refluxing conditions. Then 7.5 mL of 0.02 M sodium citrate solution was added. After reaction for 30 min, heating resource was removed and the solution was allowed to cooled down naturally to room temperature. Finally, the Au NPs were collected from the solution by centrifugation (10 000 rpm), washed with deionized water several times and redispersed in 10 mL of deionized water.

Preparation of Au@Cu_2O yolk–shell NPs with different hollow sizes

Au@Cu_2O yolk–shell NPs was prepared by hydrazine hydration reduction method.[36,38] Typically, 1 g of PVP powders was added into 10 mL of 0.01 M $Cu(NO_3)_2$ solution under constant stirring until the PVP powders dissolved completely. Then a certain amount of as-obtained Au NPs solution was added, followed by immediate introduction of trace hydrazine hydrate. After reaction, the Au@Cu_2O yolk–shell NPs were synthesized and centrifuged (10 000 rpm), washed three times with water and isopropyl alcohol, and then dried in an oven at 60 °C for later use. Au@Cu_2O NPs with different hollow sizes can be controlled through adjusting the amount of reducing agent and the reaction time (Fig. 1a).

Preparation of Cu_2O NPs

Cu_2O NPs was prepared in parallel by the same method as Au@Cu_2O yolk–shell NPs except for no addition of Au NPs and PVP powders.

Preparation of working electrode

To prepare the catalyst inks, 3 mg of catalyst powder, 10 μL of Nafion solution (5%) and 1200 μL of isopropyl alcohol were mixed and treated under sonication for 30 min. Then, 600 μL of the as-prepared ink was pipetted onto the two sides of a carbon cloth with area of 1 × 1.5 cm^2 giving a catalyst loading of 1 mg cm^{-2}.

Characterizations

X-ray diffraction (XRD) pattern was carried out on a Rigaku D/Max-2500 diffractometer equipped with a Cu Kα1 radiation (λ = 1.54 Å). Scanning electron microscopic images (SEM) were collected on a JEOL scanning electron microscope (S-4800, Japan). Transmission electron microscopic images (TEM) were obtained by a JEM-2100F microscope (JEOL, Japan) equipped with an EDS detector (Oxford Instrument, UK). X-ray photoelectron spectroscopy (XPS) was performed on an ESCALab220i-XL electron spectrometer (VG Scientific, UK) with a monochromatic Al Kα source. The gas products for CO_2 reduction were measured on a gas chromatography (GC, Agilent Technologies 7890B). The liquid products were analyzed with a Bruker AVANCE 600 using dimethyl sulphoxide (DMSO) as an internal standard.

Electrochemical performance test

Electrochemical measurements were performed on a CHI 660E electrochemical workstation in a typical H-type electrolysis cell under ambient pressure and room temperature using platinum mesh (1 × 1 cm^2) and Ag/AgCl electrode (saturated KCl) as counter and reference electrodes, respectively. The cathode and anode compartments were separated by a proton-exchange membrane (Nafion 117). The 0.1 M $KHCO_3$ aqueous solution was used as electrolyte directly without any purification. The electrode potentials were converted to the reversible hydrogen electrode reference (RHE) scale using the following Nernst equation:

$$E(\mathrm{RHE}) = E(\mathrm{Ag/AgCl}) + 0.197\ \mathrm{V} + 0.0591 \times \mathrm{pH}.$$

Before test, the catalyst was measured at −0.2 V *vs.* RHE for 30 min in Ar-saturated 0.1 M $KHCO_3$ solution to ensure all Cu_2O-shells had been reduced to Cu-shells. Then, the catalyst was immediately transfer into CO_2-saturated 0.1 M $KHCO_3$ solution to perform linear scanning voltammetry (LSV) test from 0.2 to −1.1 V *vs.* RHE until the performance of the electrode became stable. Finally, CO_2RR experiment at a constant applied voltage spanned over 3600 seconds. The electrochemically surface area (ECSA) was determined by measuring the double layer capacitance (C_{dl}), which was derived from the CV curves at various scan rates.

Analysis of CO_2 reduction products

We measure the reduction performance of the catalyst by calculating the faradaic efficiency (FE) of the CO_2 reduction

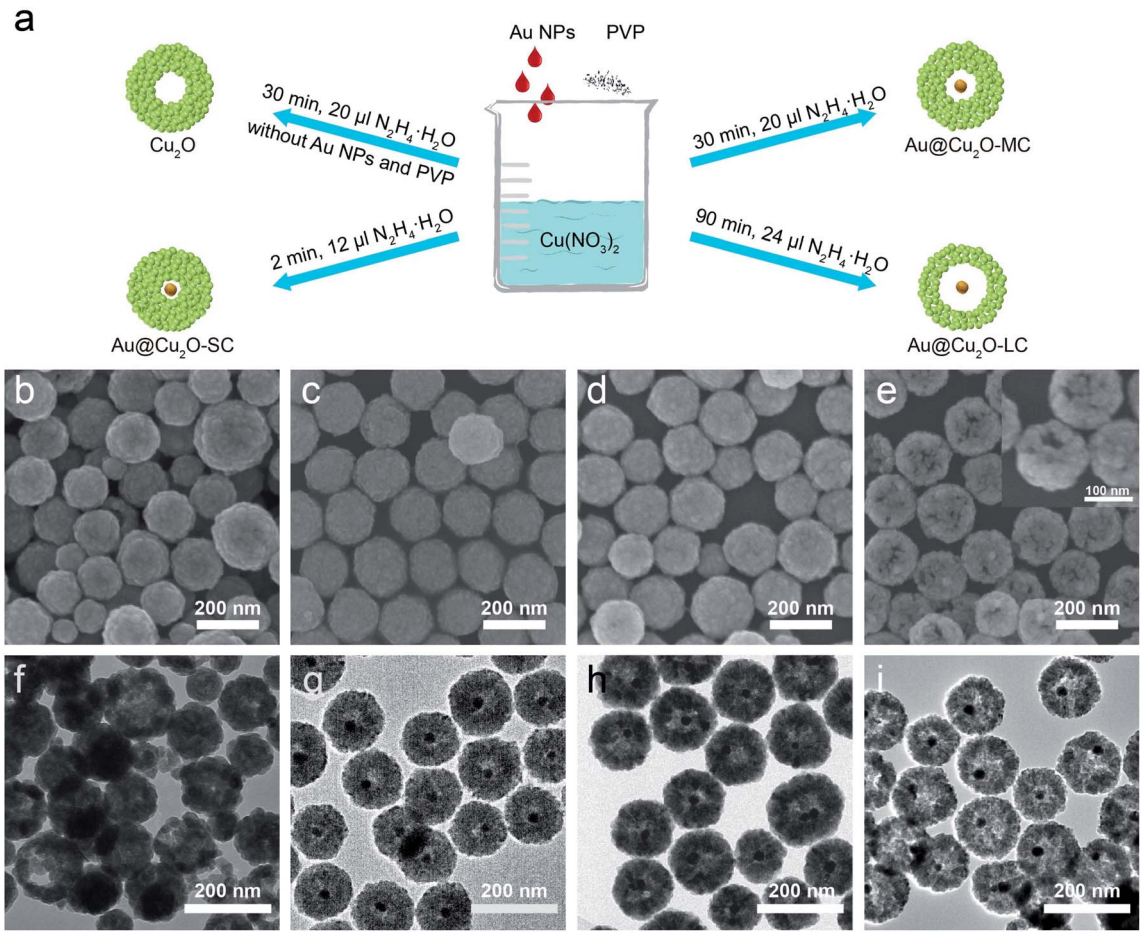

Fig. 1 (a) Schematic illustration of the synthetic process of different samples. (b–e) SEM, (f–i) TEM images of Cu_2O, Au@Cu_2O-SC, Au@Cu_2O-MC, Au@Cu_2O-LC, respectively.

product. The FE of products can be calculated using the following formula:[39]

$$FE_i = \frac{Q_i}{Q_{total}} = \frac{N_i \times n \times F}{Q_{total}}$$

i: the specific reduction product, CO, $HCOO^-$, C_2H_5OH or H_2; Q_{total}: the total charge of CO_2RR, C; Q_i: charge used for the reduction of certain product, C; N_i: number of moles for certain product, mol; n: number of electrons transferred for the CO_2-to-CO, $HCOO^-$ and C_2H_5OH conversion or water-to-H_2 reduction, which is 2, 2, 12, 2 for CO, $HCOO^-$, C_2H_5OH and H_2, respectively; F: faradaic constant, which is 96 485 C mol^{-1}.

Results and discussion

The Au NPs with uniform size and morphology were obtained according to previous literature (Fig. S1†).[36,37] Subsequently, the Au nanoparticle was encapsulated within a porous Cu_2O shell with an average size of 140 nm and the hollow size was precisely controlled by regulating the reaction time and the amount of reducing agents, as depicted in Fig. 1a. Meanwhile, Fig. S2† shows the geometry of the multilayer particle we simulated, in which the radius of the Cu_2O NPs is donated as R and the radius of the hollow size is donated as R1. In the structure, C_2 chemical selectivity can be tuned by systematically altering the R1 of 14, 35, 48 nm, which are named small cavity Au@Cu_2O (Au@Cu_2O-SC), middle cavity Au@Cu_2O (Au@Cu_2O-MC) and large cavity Au@Cu_2O (Au@Cu_2O-LC), respectively. Scanning electron microscopy (SEM) images in Fig. 1b–e reveal that the surfaces of all obtained samples are uneven, and as reaction time went on, a clear porous structure was seen on the surface of Au@Cu_2O-LC. Corresponding to SEM images, transmission electron microscopy (TEM) images in Fig. 1f–i show all the samples have a porous Cu_2O shell. And the inner hollow size became larger along with the increased reaction time and the shell structure gradually grew looser. In addition, the samples except porous Cu_2O NPs belong to yolk–shell structure and exhibit an average diameter of 140 ± 10 nm with an average Au-cores diameter of 22 ± 2 nm. Moreover, the statistical analysis based on over 100 nanoparticles indicates that they are in narrow size distribution (Fig. S3†), agreeing well with SEM and TEM results. Take Au@Cu_2O-MC catalyst for example, more detailed structural information was characterized in Fig. 2. High-resolution TEM image (HRTEM) clearly shows the lattice fringes in spacings of 0.30 and 0.25 nm corresponding to (110) and (111) planes of cubic Cu_2O

with a characteristic interplanar angel of 90° on the shell (Fig. 2a).[40] Dark-field scanning transmission electron microscopy (DF-STEM) image (Fig. 2b) exhibits the loose and porous structure of the shell material, which will promise efficient mass transport for potential electrochemical applications. Meanwhile, the corresponding energy dispersive X-ray spectroscopic (EDS) elemental mapping images (Fig. 2c–f) clearly display that Au distributes homogeneous on the core part while Cu and O are distributed mainly across the nanoparticle shell section, confirming the yolk–shell structure of Au@Cu_2O.

The composition and crystalline structure of these samples were investigated by X-ray diffraction (XRD) technique. All of the recorded diffraction peaks in the typical XRD patterns (Fig. 3a) can be well indexed to cubic Au (JCPDS no. 89-3697) and cubic Cu_2O (JCPDS no. 78-2076), corresponding to the HRTEM results. Further clues can be seen in X-ray photoelectron spectroscopic spectra (XPS) (Fig. 3b and c). By comparing the Cu 2p and Cu-LMM XPS peaks of Cu_2O and Au@Cu_2O-MC, it could be clearly seen that the Cu atom in Au@Cu_2O-MC is Cu^+, which is beneficial for CO_2RR according to previous reports.[15,16,26,41] In addition, since XPS is a surface analysis technique with investigation depth of 2–5 nm and the Au-core is coated by Cu_2O, the signal of Au element is not detected.[42] Based on these results, it can be concluded that Au-core encapsulates in porous Cu_2O-shell particle, which constitute the tandem catalyst. Consequently, it is suggested that the active Cu sites of the catalyst during CO_2RR are derived from Cu_2O.

The CO_2RR performances were evaluated over the as-obtained samples supported on the carbon cloth in 0.1 M $KHCO_3$ solution saturated with CO_2 using H-cell set-up. The products of CO_2RR were analyzed and quantified by online gas chromatography (GC) for the gas products and ^{1}H nuclear magnetic resonance spectroscopy (^{1}H NMR) for the liquid-phase products. We can determine the electrochemical activity by linear sweep voltammetry (LSV) towards CO_2RR, initially. Compared with the current density under Ar-saturated 0.1 M $KHCO_3$, it has a significant increase under CO_2-saturated electrolyte, indicating that Au@Cu_2O-MC has superior CO_2RR performance (Fig. S4a†). From Fig. S4b,† it can be seen the difference of current density between these samples, and Au@Cu_2O-MC has the maximum current density at the same potential, showing the excellent CO_2RR performance. For porous Cu_2O NPs, at low applied cathodic potential of −0.3 and −0.35 V *vs.* RHE, the only detectable product is ethanol and the faradaic efficiency ($FE_{C_2H_5OH}$) reaches 16% at −0.3 V *vs.* RHE (Fig. 4a), demonstrating the Cu_2O NPs has intrinsic C–C coupling potential. At more cathodic potentials, a substantial difference in the product distribution is found with the products of C_2 and significant increases in the CO, $HCOO^-$ production rates. After introducing Au NPs in the cavities (Fig. 4b), the selectivity shifts clearly and CO, $HCOO^-$, C_2H_5OH products are generated at −0.3 and −0.35 V *vs.* RHE. The

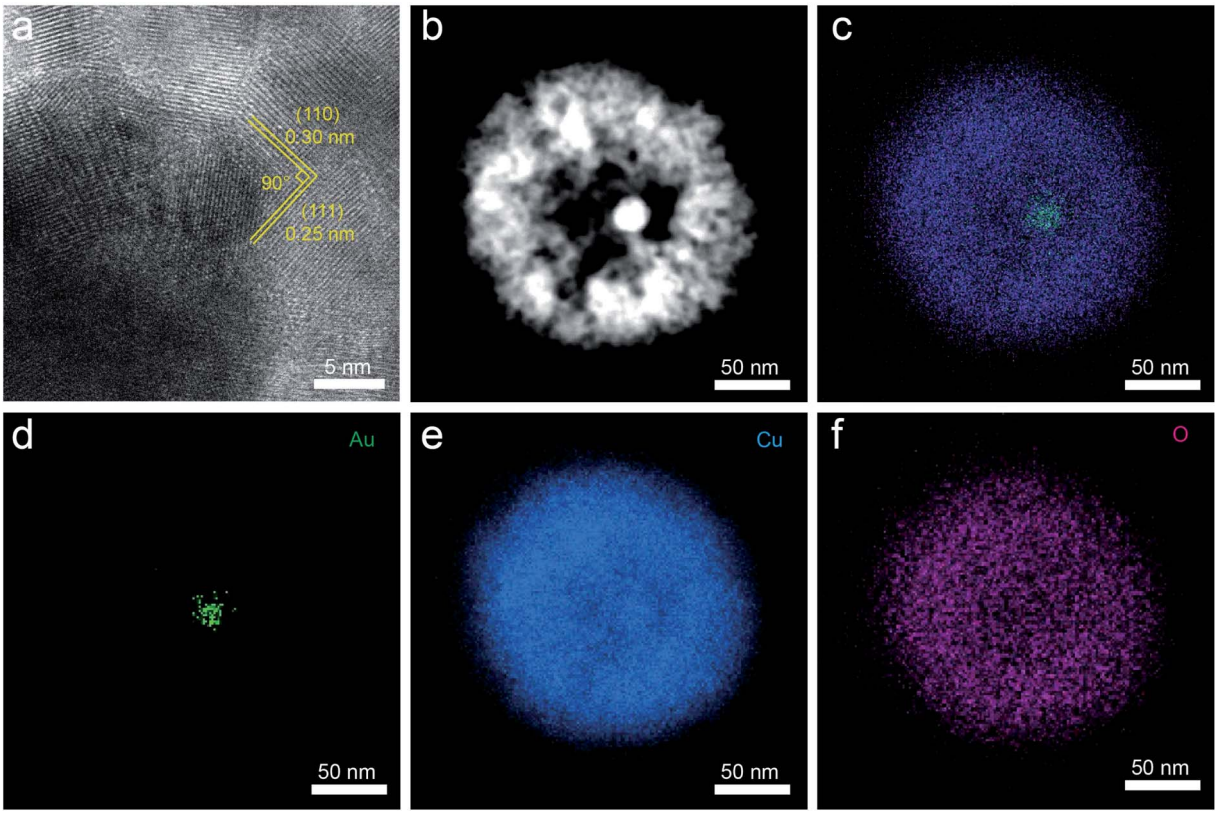

Fig. 2 (a) HRTEM, (b) DF-STEM and (c–f) EDS elemental mapping images of Au@Cu_2O-MC.

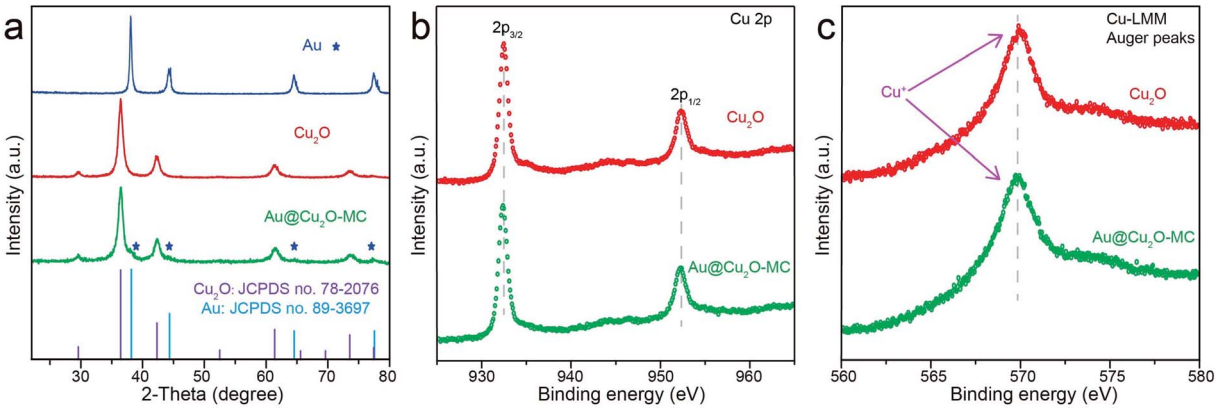

Fig. 3 (a) XRD patterns of different samples, (b) high-resolution Cu 2p and (c) Cu-LMM XPS spectra for Cu_2O and Au@Cu_2O-MC.

production of CO and HCOOH on the Au@Cu_2O-SC as well as its absence on the pure porous Cu_2O NPs, together with the promoted $FE_{C_2H_5OH}$ (36%) at low potentials, prove the effect of the suggested tandem reaction mechanism within the nano-confined space with both catalytic sites located in cavities. The Au-core is active for electroreduction of CO_2 to CO, yet the Cu-shell is able to reduce the retention of CO in the cavities to improve ethanol production (Fig. 4e). When the hollow size of the catalyst was increased to 35 nm, the largest $FE_{C_2H_5OH}$ was improved to 52.3% at −0.3 V *vs.* RHE (Fig. 4c). The reduction of the FE_{C2H5OH} at higher cathodic potentials from −0.45 to −0.6 V *vs.* RHE indicates that the previously described tandem mechanism is almost inactive in this potential window for Au@Cu_2O-MC due to the overwhelmingly competitive HER from the exposed metal species (Fig. S5†). Further increasing the hollow size to 48 nm, the largest $FE_{C_2H_5OH}$ is 38% at −0.35 V *vs.* RHE (Fig. 4d), which is slightly less than that of Au@Cu_2O-MC. However, the active potential window of tandem reaction mechanism for Au@Cu_2O-LC is broader than that of Au@Cu_2O-MC, and all of the $FE_{C_2H_5OH}$ at whole potentials from −0.27 to

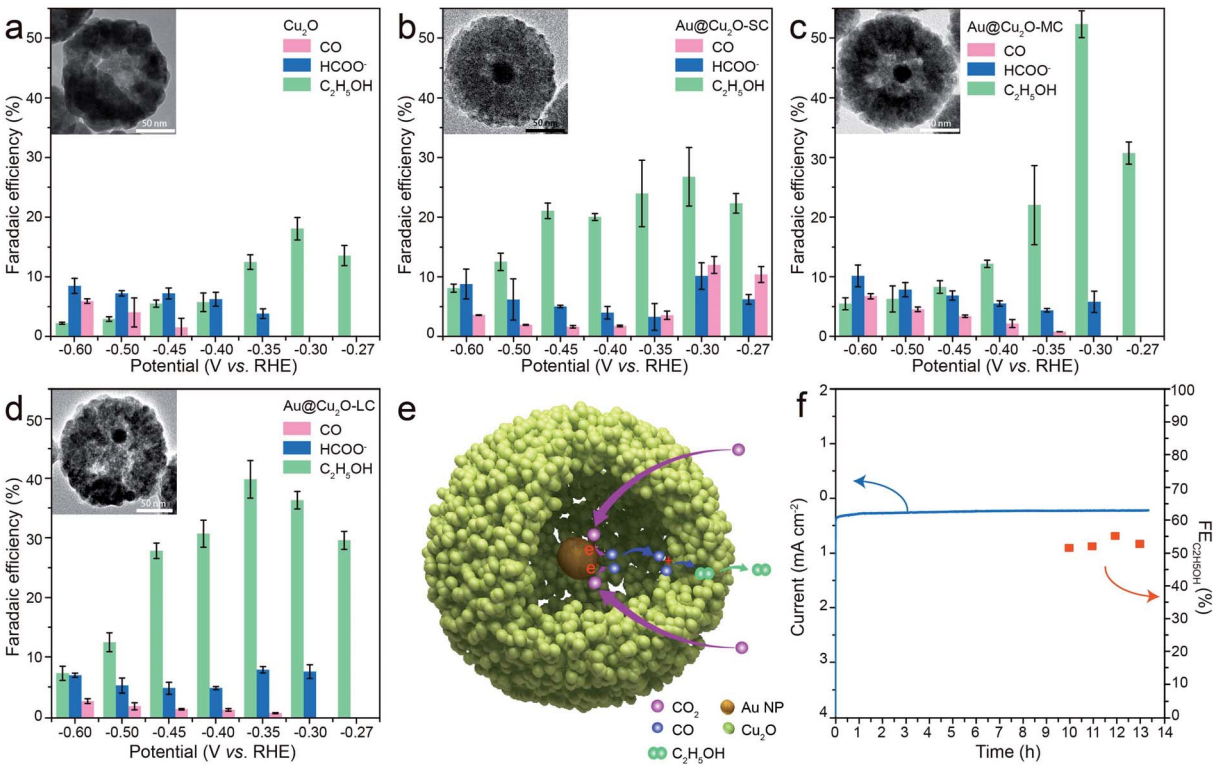

Fig. 4 (a–d) The faradaic efficiencies of carbon monoxide, formic acid, and ethanol from the CO_2RR products under a range of potentials of different samples. (e) Schematic illustration of tandem catalysis mechanism in the Au@Cu_2O cavity. (f) Time-dependent current density curve and $FE_{C_2H_5OH}$ of Au@Cu_2O-MC in CO_2-saturated 0.1 M $KHCO_3$ solution at −0.3 V *vs.* RHE.

−0.45 V *vs.* RHE is higher than that of Au@Cu_2O-SC, as well as a reduction of the detected CO at −0.27 and −0.3 V *vs.* RHE for Au@Cu_2O-MC and Au@Cu_2O-LC, suggesting the reaction mechanism of CO_2RR can be monitored *via* regulating the concentration of CO intermediate by steering the hollow size of the Cu_2O cavity.[43] Therefore, advisable hollow size for tandem reaction drove by spatial confinement effect is very important. Moreover, the ECSA of all the samples have been determined from the CV curves at different scan rates from 10 to 50 mV s^{-1} (Fig. S6†) to estimate the effect from morphology. As shown in Fig. S7,† the Au@Cu_2O-SC shows a C_{dl} value of 2.71 μF cm^{-2}, similar to 2.08 and 2.23 μF cm^{-2} of Au@Cu_2O-MC and Au@Cu_2O-LC, further verify the reaction mechanism we have proposed previously.

The durability of each catalyst was further assessed by chronoamperometry (CA) measurement since it is another important performance parameter for estimating an electrocatalyst. Fig. 4f exhibits the consecutive over 13 h CA curves at a constant potential of −0.3 V *vs.* RHE for Au@Cu_2O-MC, and it outputs a steady current density for ethanol production with a nearly unchanged $FE_{C_2H_5OH}$. The $FE_{C_2H_5OH}$ was retained >50% during the entire period, suggesting the excellent long-term durability of the catalyst, comparable with or outperforming most of other state-of-the-art Cu-based CO_2RR catalysts (Table S1†). In addition, the catalysts after CO_2RR tests were further characterized. TEM image (Fig. S8a†) and XRD pattern (Fig. S8b†) reveal that Au@Cu_2O was *in situ* electroreduction to Au@Cu, hinting that the actual active sites are from Au-core and Cu-shell, which is in agreement with previously reported results.[16,25,26]

Conclusions

In summary, we have developed a bimetallic catalyst of Au@Cu_2O yolk–shell with improved activity and selectivity for the electrochemical reduction of CO_2 to ethanol at lower potential. It was demonstrated that the spatial confinement of different active sites with a tandem catalysis mechanism leads to the selectivity shift from C_1 to C_2. The Au-core can reduce CO_2 to CO in the copper nanocavity, producing a high CO concentration, thus the Cu-shell transforms CO to ethanol production. In addition, we confine the CO concentration in the nanocavity by optimizing the hollow size of the Cu_2O nanocavity, and then perform an ethanol faradaic efficiency of 52.3% at −0.30 V *vs.* RHE. These results suggest that the present strategy may shed light on the design and preparation of highly active tandem catalysts for other electrochemical reactions.

Conflicts of interest

There are no conflicts to declare.

Acknowledgements

This work was supported by the Fundamental Research Funds for the Central Universities (No. 2018JBM067) and the National Natural Science Foundation of China (No. 21603011).

Notes and references

1 S. Lin, C. S. Diercks, Y.-B. Zhang, N. Kornienko, E. M. Nichols, Y. Zhao, A. R. Paris, D. Kim, P. Yang and O. M. Yaghi, *Science*, 2015, **349**, 1208–1213.
2 W. Bi, C. Wu and Y. Xie, *ACS Energy Lett.*, 2018, **3**, 624–633.
3 X. Liu, J. Iocozzia, Y. Wang, X. Cui, Y. Chen, S. Zhao, Z. Li and Z. Lin, *Energy Environ. Sci.*, 2017, **10**, 402–434.
4 R. Francke, B. Schille and M. Roemelt, *Chem. Rev.*, 2018, **118**, 4631–4701.
5 L.-q. He, H. Yang, J.-j. Huang, X.-h. Lu, G.-r. Li, X.-q. Liu, P.-p. Fang and Y.-x. Tong, *RSC Adv.*, 2019, **9**, 10168–10173.
6 H. B. Yang, S.-F. Hung, S. Liu, K. Yuan, S. Miao, L. Zhang, X. Huang, H.-Y. Wang, W. Cai, R. Chen, J. Gao, X. Yang, W. Chen, Y. Huang, H. M. Chen, C. M. Li, T. Zhang and B. Liu, *Nat. Energy*, 2018, **3**, 140–147.
7 K. P. Kuhl, E. R. Cave, D. N. Abram and T. F. Jaramillo, *Energy Environ. Sci.*, 2012, **5**, 7050–7059.
8 C.-T. Dinh, T. Burdyny, M. G. Kibria, A. Seifitokaldani, C. M. Gabardo, F. P. G. de Arquer, A. Kiani, J. P. Edwards, P. De Luna and O. S. Bushuyev, *Science*, 2018, **360**, 783–787.
9 F. J. Gomez, G. Chumanov, M. F. Silva and C. D. Garcia, *RSC Adv.*, 2019, **9**, 33657–33663.
10 Y. X. Duan, F. L. Meng, K. H. Liu, S. S. Yi, S. J. Li, J. M. Yan and Q. Jiang, *Adv. Mater.*, 2018, **30**, e1706194.
11 Y. Song, W. Chen, C. Zhao, S. Li, W. Wei and Y. Sun, *Angew. Chem., Int. Ed.*, 2017, **56**, 10840–10844.
12 Q. Li, W. Zhu, J. Fu, H. Zhang, G. Wu and S. Sun, *Nano Energy*, 2016, **24**, 1–9.
13 C. M. Gabardo, C. P. O'Brien, J. P. Edwards, C. McCallum, Y. Xu, C.-T. Dinh, J. Li, E. H. Sargent and D. Sinton, *Joule*, 2019, **3**, 2777–2791.
14 C. Xie, C. Chen, Y. Yu, J. Su, Y. Li, G. A. Somorjai and P. Yang, *Nano Lett.*, 2017, **17**, 3798–3802.
15 M. G. Kibria, C. T. Dinh, A. Seifitokaldani, P. De Luna, T. Burdyny, R. Quintero-Bermudez, M. B. Ross, O. S. Bushuyev, F. P. Garcia de Arquer, P. Yang, D. Sinton and E. H. Sargent, *Adv. Mater.*, 2018, **30**, e1804867.
16 T.-T. Zhuang, Y. Pang, Z.-Q. Liang, Z. Wang, Y. Li, C.-S. Tan, J. Li, C. T. Dinh, P. De Luna, P.-L. Hsieh, T. Burdyny, H.-H. Li, M. Liu, Y. Wang, F. Li, A. Proppe, A. Johnston, D.-H. Nam, Z.-Y. Wu, Y.-R. Zheng, A. H. Ip, H. Tan, L.-J. Chen, S.-H. Yu, S. O. Kelley, D. Sinton and E. H. Sargent, *Nat. Catal.*, 2018, **1**, 946–951.
17 D. Kim, C. S. Kley, Y. Li and P. Yang, *Proc. Natl. Acad. Sci. U. S. A.*, 2017, **114**, 10560–10565.
18 Y. Jiao, Y. Zheng, P. Chen, M. Jaroniec and S. Z. Qiao, *J. Am. Chem. Soc.*, 2017, **139**, 18093–18100.
19 Y. Zhou, F. Che, M. Liu, C. Zou, Z. Liang, P. De Luna, H. Yuan, J. Li, Z. Wang, H. Xie, H. Li, P. Chen, E. Bladt, R. Quintero-Bermudez, T. K. Sham, S. Bals, J. Hofkens, D. Sinton, G. Chen and E. H. Sargent, *Nat. Chem.*, 2018, **10**, 974–980.
20 S. Zhong, X. Yang, Z. Cao, X. Dong, S. M. Kozlov, L. Falivene, J. K. Huang, X. Zhou, M. N. Hedhili, Z. Lai, K. W. Huang,

Y. Han, L. Cavallo and L. J. Li, *Chem. Commun.*, 2018, **54**, 11324–11327.
21 K. D. Yang, W. R. Ko, J. H. Lee, S. J. Kim, H. Lee, M. H. Lee and K. T. Nam, *Angew. Chem., Int. Ed.*, 2017, **56**, 796–800.
22 Y. Hori, I. Takahashi, O. Koga and N. Hoshi, *J. Phys. Chem. B*, 2002, **106**, 15–17.
23 T.-T. Zhuang, Z.-Q. Liang, A. Seifitokaldani, Y. Li, P. De Luna, T. Burdyny, F. Che, F. Meng, Y. Min, R. Quintero-Bermudez, C. T. Dinh, Y. Pang, M. Zhong, B. Zhang, J. Li, P.-N. Chen, X.-L. Zheng, H. Liang, W.-N. Ge, B.-J. Ye, D. Sinton, S.-H. Yu and E. H. Sargent, *Nat. Catal.*, 2018, **1**, 421–428.
24 P. B. O'Mara, P. Wilde, T. M. Benedetti, C. Andronescu, S. Cheong, J. J. Gooding, R. D. Tilley and W. Schuhmann, *J. Am. Chem. Soc.*, 2019, **141**, 14093–14097.
25 C. G. Morales-Guio, E. R. Cave, S. A. Nitopi, J. T. Feaster, L. Wang, K. P. Kuhl, A. Jackson, N. C. Johnson, D. N. Abram, T. Hatsukade, C. Hahn and T. F. Jaramillo, *Nat. Catal.*, 2018, **1**, 764–771.
26 C. W. Li, J. Ciston and M. W. Kanan, *Nature*, 2014, **508**, 504–507.
27 T. Le, A. Striolo, C. H. Turner and D. R. Cole, *Sci. Rep.*, 2017, **7**, 1–12.
28 Y. Liu, X.-Y. Yu, Y. Fang, X. Zhu, J. Bao, X. Zhou and X. W. D. Lou, *Joule*, 2018, **2**, 725–735.
29 P. Han, Z. Wang, M. Kuang, Y. Wang, J. Liu, L. Hu, L. Qian and G. Zheng, *Adv. Energy Mater.*, 2018, **8**, 1801230.
30 L. Tang, X. Meng, D. Deng and X. Bao, *Adv. Mater.*, 2019, **31**, e1901996.
31 W. Zhu, Y.-J. Zhang, H. Zhang, H. Lv, Q. Li, R. Michalsky, A. A. Peterson and S. Sun, *J. Am. Chem. Soc.*, 2014, **136**, 16132–16135.
32 S. Mezzavilla, S. Horch, I. E. L. Stephens, B. Seger and I. Chorkendorff, *Angew. Chem., Int. Ed.*, 2019, **58**, 3774–3778.
33 A. Verdaguer-Casadevall, C. W. Li, T. P. Johansson, S. B. Scott, J. T. McKeown, M. Kumar, I. E. Stephens, M. W. Kanan and I. Chorkendorff, *J. Am. Chem. Soc.*, 2015, **137**, 9808–9811.
34 A. Loiudice, P. Lobaccaro, E. A. Kamali, T. Thao, B. H. Huang, J. W. Ager and R. Buonsanti, *Angew. Chem., Int. Ed.*, 2016, **55**, 5789–5792.
35 M. Fan, Z. Bai, Q. Zhang, C. Ma, X.-D. Zhou and J. Qiao, *RSC Adv.*, 2014, **4**, 44583–44591.
36 L. Zhang, D. A. Blom and H. Wang, *Chem. Mater.*, 2011, **23**, 4587–4598.
37 X. Ji, X. Song, J. Li, Y. Bai, W. Yang and X. Peng, *J. Am. Chem. Soc.*, 2007, **129**, 13939–13948.
38 J. Zhang, G. Liu, F. He, L. Chen and Y. Huang, *RSC Adv.*, 2015, **5**, 87903–87907.
39 C. He, Y. Zhang, Y. Zhang, L. Zhao, L.-P. Yuan, J. Zhang, J. Ma and J.-S. Hu, *Angew. Chem., Int. Ed.*, 2020, **59**, 4914–4919.
40 Y. Shang, D. Sun, Y. Shao, D. Zhang, L. Guo and S. Yang, *Chem.–Eur. J.*, 2012, **18**, 14261–14266.
41 Y. Lum, B. Yue, P. Lobaccaro, A. T. Bell and J. W. Ager, *J. Phys. Chem. C*, 2017, **121**, 14191–14203.
42 P. J. Cumpson, *Appl. Surf. Sci.*, 1999, **144**, 16–20.
43 J. Li, Z. Wang, C. McCallum, Y. Xu, F. Li, Y. Wang, C. M. Gabardo, C.-T. Dinh, T.-T. Zhuang, L. Wang, J. Y. Howe, Y. Ren, E. H. Sargent and D. Sinton, *Nat. Catal.*, 2019, **2**, 1124–1131.